Journal of The Electrochemical Society, **161** (10) F969-F976 (2014)
0013-4651/2014/161(10)/F969/8/$31.00 © The Electrochemical Society

Effect of Pr-Doping on Structural, Electrical, Thermodynamic, and Mechanical Properties of $BaCeO_{3-\delta}$ as Proton Conductor

J. F. Basbus,[a] M. Moreno,[b] A. Caneiro,[b] and L. V. Mogni[b,*,z]

[a]*CNEA-AGNPCyT, Centro Atomico Bariloche, S. C. de Bariloche, Rio Negro 8400, Argentina*
[b]*CNEA-CONICET, Centro Atomico Bariloche, S. C. de Bariloche, Rio Negro 8400, Argentina*

The effect of partial substitution of Ce by Pr ions in $BaCe_{1-x}Pr_xO_{3-\delta}$ ($0 \leq x \leq 0.8$) perovskite was studied to improve the proton conductor capability, including transport and mechanical properties, thermodynamic stability, CO_2 tolerance and sintering. The stability under oxidizing and reducing (5% H_2/Ar and 10% CO_2/Ar) atmospheres was evaluated by thermogravimetry. The conductivity was studied by Electrical Impedance Spectroscopy (EIS) under wet (2% H_2O) flow of 20% O_2/Ar and 10% H_2/Ar as a function of temperature between 100 and 600°C. The mechanical stiffness and fracture load were measured by a Small Punch Testing (SPT) method at room temperature. It was found that the Pr doping improves the sintering capacity, and increases the conductivity. However, the stability under reducing and carbon dioxide atmospheres decreases. A correlation between electrical conductivity, CO_2 tolerance, thermodynamic stability under reducing atmospheres and mechanical properties was found. Dense $BaCe_{0.8}Pr_{0.2}O_{3-\delta}$ obtained at 1350°C presents low porosity (5 ± 1%), an improvement of 30% in stiffness and 56% in fracture load, good stability under oxidizing and reducing atmosphere, slightly higher CO_2 tolerance range and an increase of electrical conductivity respect to that of the un-doped compound.

Manuscript submitted April 16, 2014; revised manuscript received June 23, 2014. Published July 3, 2014. This was Paper 739 presented at the San Francisco, California, Meeting of the Society, October 27–November 1, 2013.

Solid oxide fuel cells (SOFCs) are efficient devices for energy conversion with low environmental impact.[1–5] However, their high operating temperatures (800–1000°C), affects the long term stability and durability.[6,7] Solid oxide fuel cells based on a proton-conducting oxide electrolyte (PC-SOFC) may be a solution of these issues, due to the low temperature operating range (400–800°C).[8–11]

Barium cerate-based materials are promising electrolytes for PC-SOFC.[12–14] Nevertheless, the undoped $BaCeO_3$ perovskite presents high sintering temperature, poor CO_2 tolerance and relatively low conductivity.[15–17] To overcome these drawbacks, different strategies are briefly discussed.

The formation of oxygen vacancies on barium cerates are promoted under H_2-rich atmospheres due to the partial reduction of Ce^{4+} to Ce^{3+}. On the presence of water vapor, the oxygen vacancies are filled with H_2O molecules and locating the protons in interstitials sites. These interstitial protons can jump through oxygen-structure sites promoting the H-conduction[18,19]

$$V_o^{\bullet\bullet} + H_2O + O_o^x \rightarrow 2OH_o^{\bullet} \quad [1]$$

The proton conduction mechanism is characterized by a low activation energy[20] and a high proton solubility at lower temperatures.[21,22] These main features characterize a good electrolyte at low temperatures. The partial substitution of cerium sites by lanthanides or transition metal trivalent oxides induces the oxygen vacancies formation according to the following defect reaction:

$$2Ce_{Ce}^x + Ln_2O_3 + O_o^x \rightarrow V_o^{\bullet\bullet} + 2Ln'_{Ce} + 2CeO_2 \quad [2]$$

A previous study on the effect of trivalent lanthanide doping shows that the highest conductivity is achieved for a Gd-doped compound.[23,24] Despite this report, lanthanides doping contributions are controversial, either enhancing proton conductivity[25] or promoting the opposite effect[26,27]

At operating conditions, the electrolyte must be a high density material in order to prevent the mixing between the gases coming from both anode and cathode. Many efforts are focused to obtain dense samples at lower temperatures either by doping with Zr, Gd, Y and Yb,[28–31] or by adding non-refractory oxides, such as ZnO.[32] The electrical transport properties are strongly affected by the grain size and the grains connectivity. Then the microstructure is the key to improve the conduction trough the bulk and grain boundary.[33] Sintering features also affect the mechanical properties[34] which are a fundamental issue in the design of the electrolyte supported SOFC.

The stability of electrolytes in CO_2-containing atmospheres is also a challenge because the $BaCO_3$ formation is a drawback for the ionic conductivity of the structure and also leads to mechanical degradation.[35,36] Different strategies are used to solve this issue. For example, some representative compositions such as $BaCe_{0.9}Y_{0.1}O_{2.95}$,[37] $BaCe_{0.4}Zr_{0.4}Y_{0.2}O_{3-\delta}$[38] and $BaCe_{0.9-x}Zr_xY_{0.1}O_{3-\delta}$ with $x \geq 3$[39] present a high tolerance to CO_2. Despite the improvement, conductivity is decreased in these materials. A novel strategy is based on the protection of the highly but unstable proton conducting electrolyte by deposition of a chemically stable buffer layer on the proton electrolyte, such as the $BaZr_{0.4}Ce_{0.4}Y_{0.2}O_{3-\delta}$-$BaCe_{0.8}Y_{0.2}O_{3-\delta}$ dual-layer system.[40]

Up to date, no systematic study of the effect of the partial substitution of Ce by Pr ions is previously reported. In this work, the $BaCe_{1-x}Pr_xO_{3-\delta}$ ($x = 0$, 0.2, 0.4, 0.6 and 0.8) series is studied to evaluate the effect of Pr doping on microstructural, structural, mechanical, electrical and the stability of this oxides as candidates to be used as PC-SOFC electrolyte.

Experimental

Sample preparation.— Dense electrolytes were obtained through Pechini-modified method. The starting materials, $Ba(NO_3)_2$, Pr_6O_{11}, and $Ce(NO_3)_3.6H_2O$, were dissolved using EDTA and citric acid as quelating agents in a molar ratio metal: EDTA:Citric acid of 1:1:1.5. The pH was tuned to 10 using ammonium hydroxide. The polymerization was induced by heating at 100°C. The obtained polymers were heated to produce self-combustion at approximately 200°C. Two pretreatments were performed heating the samples at 400°C and 900°C for 6 and 12 h, respectively. The final product was uniaxially pressed at 50 kg/cm^2 and sintered at 1350°C for 12 h. The samples were ball milled and powders were dehydrated by annealing in dry N_2 at 800°C for 24 h. The phase purity was evaluated by XRD using a PANalytical Empyrean diffractometer.

Structural characterization.— The crystal structure of powders were studied by X-Ray Diffraction (XRD) with synchrotron radiation at 10 keV (XPD beamline of LNLS-Campinas, Brazil). The crystalline structures were refined fitting the structural parameters of $BaCeO_3$[41] and $BaCe_{0.85}Pr_{0.15}O_3$[42] by Rietveld method using Fullprof software.[43]

Microstructural characterization.— The microstructure of dense pellets were observed by Scanning Electronic Microscopy (SEM) with a Philips 515 microscope. Elementary analysis was performed by energy dispersive spectrometry (EDS). The porosity was analyzed

*Electrochemical Society Active Member.
zE-mail: mogni@cab.cnea.gov.ar

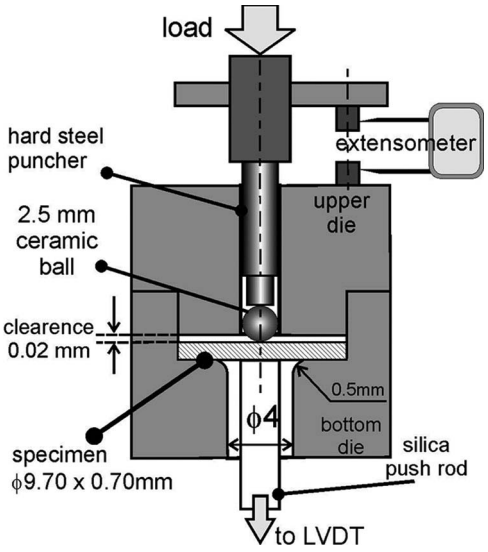

Figure 1. Small punch test holder.

from SEM images of cross section of polished samples using ImageTool3 software.[44,45] The dense polished pellets were thermally etched at 1150°C for 1 h to reveal the grain boundaries of the sintered bodies and to measure the grain size.

Stability tests.— The thermodynamic stability of compounds under oxidizing and reducing atmosphere was studied by thermogravimetry (TG) using a Cahn 1000 electrobalance.[46] The% of mass variation (% Weight) respect to the initial mass was analyzing as a function of temperature between 100 and 800°C in 20% O_2/Ar and 5% H_2/Ar atmospheres. The% weight data were evaluated under equilibrium conditions (not mas change with time at constant temperature). The resistance to the carbonation was evaluated under accelerating condition by TG with a gas mixture of 10% CO_2/Ar. The non isothermal measurement was done between room temperature and 900°C with a heating rate of 5°C/min. XRD data were collected at room temperature on samples exposed to this atmosphere and cooled in Ar.

Mechanical test.— The effect of Pr doping on the mechanical properties were also evaluated at room temperature on sintered samples using the Small Punch Testing (SPT) method.[47,48] In this study, dense disks of specimens of 9.8 mm of diameter and 0.7 mm (+–5 microns of tolerance) of thickness were carefully polished and located in a specially designed holder (see Figure 1), with a clearance of about 200 microns between top face of specimen and upper die. This gap prevents a premature fracture due to clamping. The load was applied through a hard steel puncher pushing a 2.5 mm. silicon nitride ball used as indenter. The SPT equipment was loaded by a universal testing machine Instron 5567 with a load cell of 0.5 kN. Two displacements were recorded during each test: i- the puncher displacement was measured by an extensometer model MTS of 12.5 mm of gage length, and ii- displacement of bottom side of the specimen was measured by a linear variable differential transducer (LVDT) linked by a silica push rod. The tests were performed in air at room temperature under constant crosshead speed of 0.05 mm/min up to the fracture. Each composition were tested by triplicate.

Electrical characterization.— The electrical conductivity of dense sample were determined by Electrochemical Impedance Spectroscopy (EIS). Dense disk of samples were painted on both sides with Pt ink. The EIS spectra were collected between 100 and 600°C under wet (2% H_2O) synthetic air (20% O_2/Ar) and wet dilute hydrogen (10% H_2/Ar) flow, using an Autolab PGSTAT30 potentiostat. The spectra were collected between 1 MHz and 0.1 Hz, with 50 mV of amplitude.

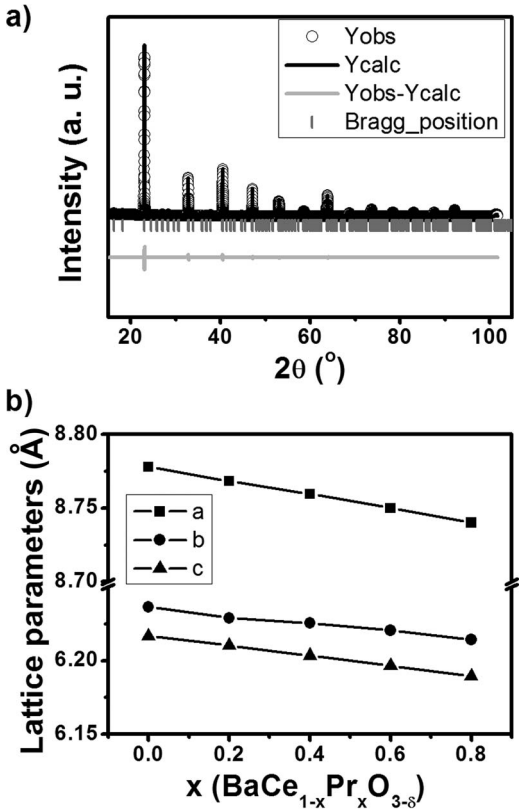

Figure 2. a) Measured XRD pattern (Yobs) and Rietveld refinement (Ycalc) and difference between both at 10 keV for $BaCe_{0.6}Pr_{0.4}O_{3-\delta}$ perovskite. Bragg positions are also included. b) Lattice parameters for the orthorhombic phase (*a*, *b* and *c*) as function of Pr content.

The EIS spectra were fitted with an electrical equivalent circuit using the Zview software.[49]

Results and Discussion

Samples characterization.— XRD data show that Pr doping samples are single phase within the whole range of compositions. This phase is described by the orthorhombic space group *Pmcn*, N° 62. As an example, Figure 2a shows the diffraction pattern of the $BaCe_{0.6}Pr_{0.4}O_{3-\delta}$ perovskite and Table I summarizes the cell parameters of each composition. Orthorhombic lattice parameters (*a*, *b* and *c*) decrease as the Pr content increases (see Figure 2b). A ratio of Pr^{+4} / $Pr^{+3} = 2$ is present in the starting Pr_6O_{11}. Then, it could be expected that Pr^{+4} ions may substitute Ce^{+4} in B sites ($r_{Ce+4}{}^{VI} = 0.87$ Å and $r_{Pr+4}{}^{VI} = 0.85$ Å) and Pr^{+3} could partially replaces both, Ba^{+2} in A site ($r_{Ba+2}{}^{XII} = 1.61$ Å) and Ce^{+4} in B site ($r_{Pr+3}{}^{VI} = 0.99$ Å).[50] It is expected that the replacement of Ce^{4+} by Pr^{3+} predominates over that of Ba^{2+} by Pr^{3+} substitution due to the nominal oxide compositions. The change of lattice parameters with Pr content suggest that the two effects may reduce the structure volume due to:

Table I. Lattice parameters of orthorhombic *Pmcn* perovskites.

$BaCe_{1-x}Pr_xO_{3-\delta}$ x	a (Å)	b (Å)	c (Å)
0	8.77789	6.23629	6.21664
0.2	8.76826	6.22886	6.21025
0.4	8.75952	6.22537	6.20345
0.6	8.74999	6.22045	6.19647
0.8	8.74009	6.21421	6.18949

1. A reduction of the mean ionic radii in B site since Pr^{+4} has a slightly smaller ionic radii than that of the Ce^{+4},
2. The creation of oxygen vacancies induced by the charge compensation of Pr^{+3} ions which could distort the lattice by preserving the symmetry.

As an example, Figure 3a shows a polished cross-section SEM image of $BaCe_{0.2}Pr_{0.8}O_{3-\delta}$ sample. The% porosity of dense electrolytes is obtained using ImageTool3 software.[45] These values and average grain size as a function of Pr doping are shown in Figure 3c. The Pechini modified method allowed to obtain samples with density higher than 90% at 1350°C. This sintering temperature is 350°C lower than those reported for dense samples of $BaCe_{0.85}Ln_{0.15}O_{3-\delta}$ (Ln = Gd, Y, Yb) prepared by solid state reaction[28] and 150°C below that of $BaCe_{0.8-x}Zr_xY_{0.2}O_{3-\delta}$ obtained by free-nitrate acetate - H_2O_2 combustion method.[30] From Figure 3c, it is also observed that low levels of Pr-doping are enough to decrease the porosity and improve the sintering. Grain sizes of dense samples were measured after the thermal etch by the line intersection method. Figure 3b shows a SEM image of $BaCe_{0.2}Pr_{0.8}O_{3-\delta}$ etched sample. The phase segregation on grain boundary produced during thermal etching, facilitates the grain size evaluation. The apparent phase segregation is a surface effect. This was confirmed by SEM analysis on the fracture surface of a sample after the thermal etching was performed. All samples present a homogenous grain size distribution. It increases as Pr content does. Then, the Pr content improves the capability to obtain dense samples, lowering the porosity and promoting grain growth.

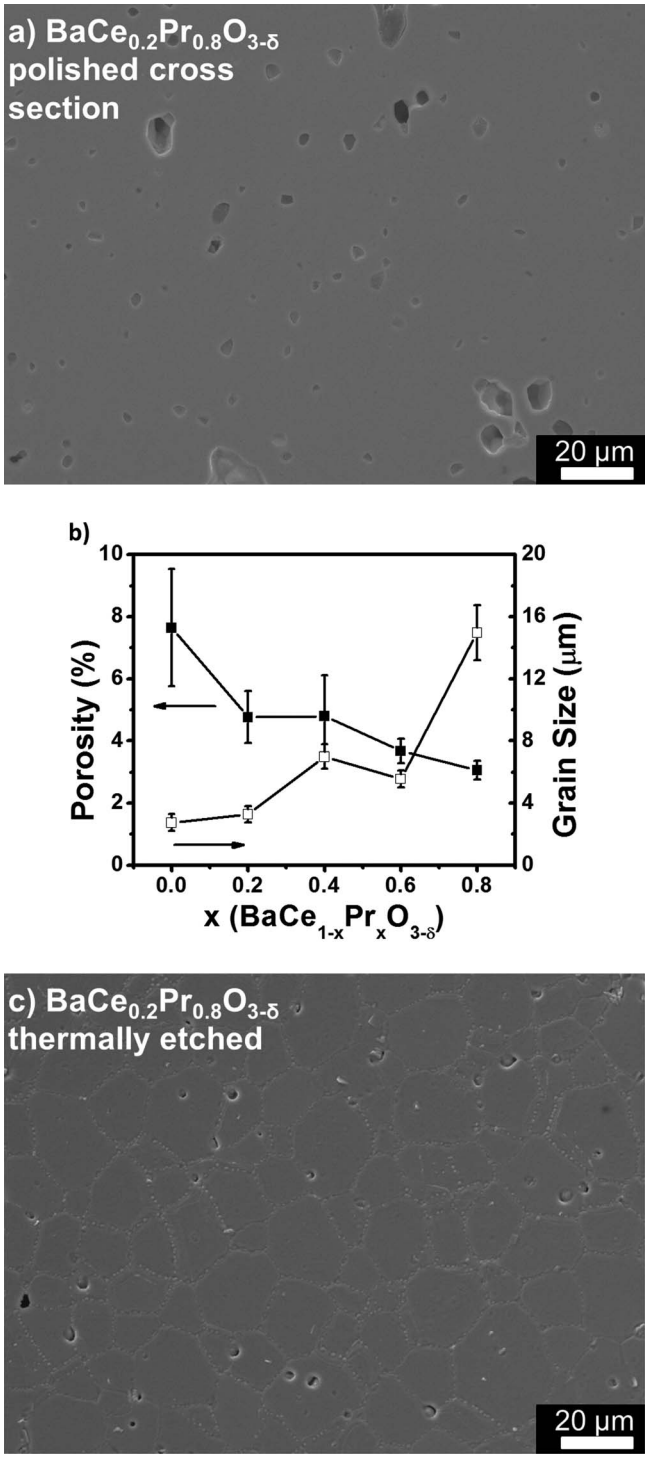

Figure 3. SEM image of $BaCe_{0.2}Pr_{0.8}O_{3-\delta}$ dense pellet sintered at 1350°C: a) polished cross section and b) surface thermally etched. From the SEM images, the c) porosity% and grain size mean distribution is obtained as a function of Pr content.

Thermodynamic stability.— For the selected applications, it is essential to ensure the thermodynamic stability of electrolytes under typical PC-SOFC operation conditions: 400–600°C and under reducing atmosphere H_2-rich in anode side or oxidizing atmosphere with O_2 in cathode side. The CO_2 tolerance must be also guaranteed due to the basicity of Ba and the presence of impurities in fuels. The accelerated aging tests (higher temperatures or high gas concentrations) are useful since they reduce experimental time and allow evaluating long period processes. The% weight change as a function of temperature are shown in Figure 4a for $BaCe_{0.2}Pr_{0.8}O_{3-\delta}$. Measurements were done

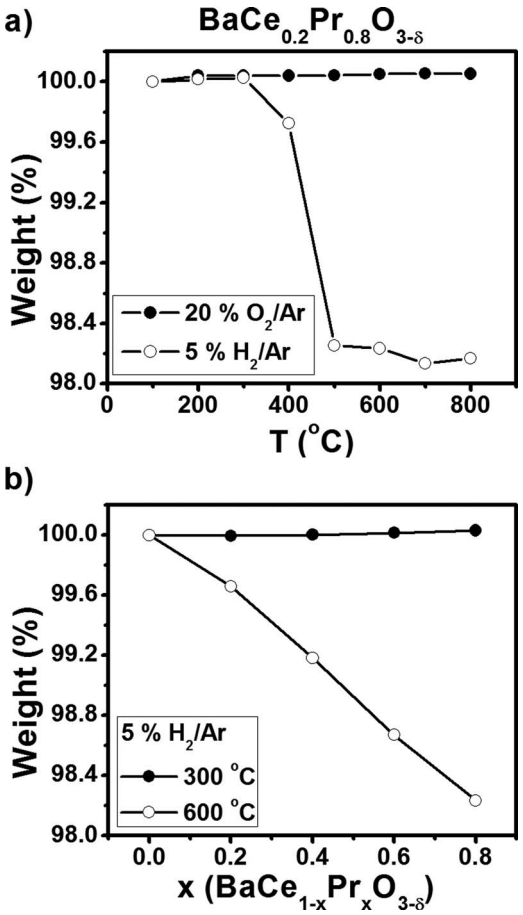

Figure 4. % Weight as function of temperature under 20% O_2/Ar and 5% H_2/Ar for a) $BaCe_{0.2}Pr_{0.8}O_{3-\delta}$. b)% Weight as function of the Pr content at 300 and 600°C under 5% H_2/Ar.

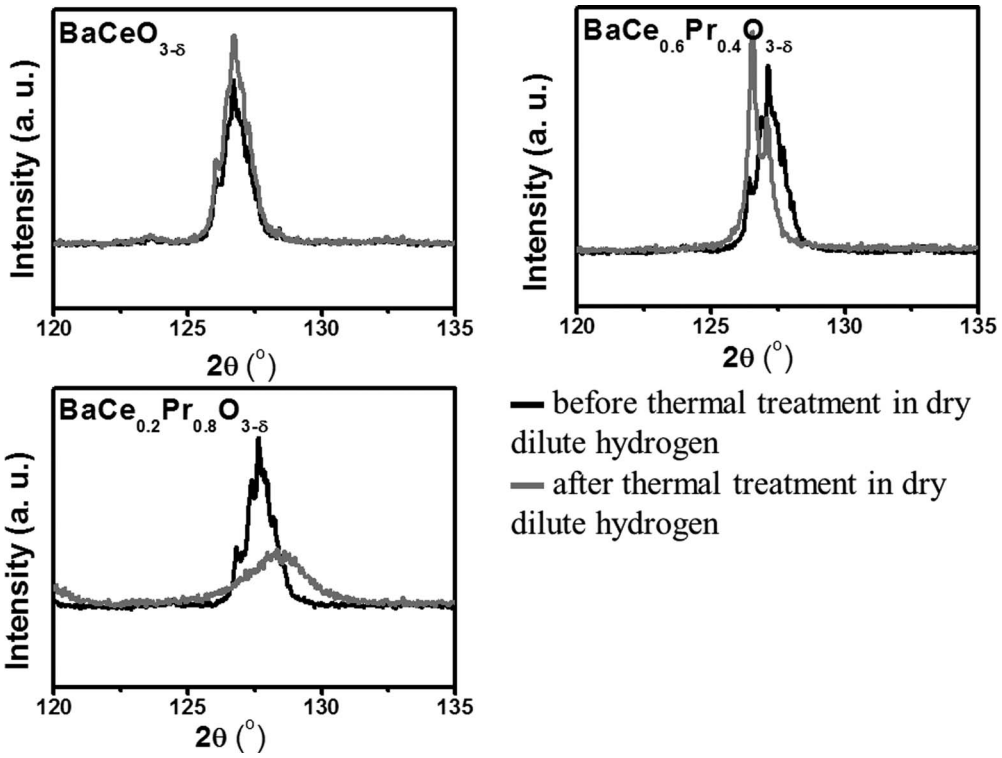

Figure 5. XRD patterns between 120 and 135° for $BaCe_{1-x}Pr_xO_{3-\delta}$ (x = 0, 0.4 and 0.8) samples before and after heating at 800°C in dry 10% H_2/Ar (diluted hydrogen) for 12 h.

under dry synthetic air and 5% H_2/Ar gas mixture. No mass change was detected for all $BaCe_{1.x}Pr_xO_{3-\delta}$ compositions under dry synthetic air between 100 and 800°C. However, the $BaCe_{0.8}Pr_{0.2}O_{3-\delta}$ compound is reduced above 500°C in 5% H_2/Ar flow. Figure 4b show the% weight as function of the Pr content, at 300 and 600°C under 5% H_2/Ar flow. The% weight loss at 600°C under 5% H_2/Ar increases with Pr content suggesting a partial reduction of Pr^{+4} into Pr^{+3}. To evaluate if Pr^{+4} reduction affects the thermodynamic stability and the crystal structure of $BaCe_{1-x}Pr_xO_{3-\delta,}$ XRD data were collected on $BaCe_{1-x}Pr_xO_{3-\delta}$ powders before and after a heat-treatment at 800°C during 12 h in 10% H_2/Ar atmosphere. Figure 5 shows a comparison between XRD data collected in the high angle region (2θ ∼ 120–135°) before and after this treatment. From the complete diffraction patterns, it was concluded that $BaCeO_{3-\delta}$ and $BaCe_{0.8}Pr_{0.2}O_{3-\delta}$ preserve the orthorhombic structure while $BaCe_{0.6}Pr_{0.4}O_{3-\delta}$ and $BaCe_{0.4}Pr_{0.6}O_{3-\delta}$ change the crystal symmetry. $BaCe_{0.2}Pr_{0.8}O_{3-\delta}$ shows peak broadening due to sample amorphization. These results suggest that Pr content decreases the stability of $BaCe_{1-x}Pr_xO_{3-\delta}$ compounds under reducing atmosphere above 400°C. In the cases where a change of symmetry was detected, an estimation of the new lattice parameters was performed using the Le Bail method.[51] A volume expansion larger than 12% was observed for x = 0.4, 0.6 compositions after the heat-treatment in hydrogen. This result agrees with previous studies of phase stability on $BaZr_{0.9-x}Pr_xGd_{0.1}O_{3-\delta}$ (x = 0.3 and 0.6) compounds.[52] The mass change and crystal structure affects the mechanical integrity of dense pellets due to cracks formation.

The stability under CO_2-rich atmosphere was evaluated by TG. A mass gain indicates a degradation of the samples due to $BaCO_3$ formation. Figure 6a shows the% weight as a function of temperature under 10% CO_2-Ar gas mixture. All compositions were stable (not change in mass) until 500°C. From 550 to 850°C, a mass gain indicates decomposition of the sample due to the formation of $BaCO_3$. At T > 850°C the mass of $BaCeO_{3-\delta}$ and $BaCe_{0.8}Pr_{0.2}O_{3-\delta}$ decreases indicating the decomposition of $BaCO_3$ while for Pr reach samples the mass remains constant. This behavior was confirmed by XRD in samples obtained after CO_2 exposition by cooling under Ar. XRD patterns of $BaCeO_{3-\delta}$ carbonated samples shown mainly the presence of the perovskite phase, and small amounts of CeO_2 and $BaCO_3$ while $BaCe_{0.8}Pr_{0.2}O_{3-\delta}$ presents significant amounts of CeO_2, Pr_6O_{11} and $BaCO_3$, in addition to the perovskite phase. On the other hand, $BaCe_{0.6}Pr_{0.4}O_{3-\delta}$, $BaCe_{0.4}Pr_{0.6}O_{3-\delta}$ and $BaCe_{0.2}Pr_{0.8}O_{3-\delta}$ were irreversible decomposed into a mixture of $BaCO_{3,}$ CeO_2, Pr_6O_{11} and other non-identified oxides. Figure 6b and 6c show% weight gain as a function of the Pr content and the diffraction patterns of $BaCe_{0.8}Pr_{0.2}O_{3-\delta}$ and $BaCe_{0.2}Pr_{0.8}O_{3-\delta}$ after the carbonation with the subsequent cooling in Ar, respectively. It is evident that the CO_2 tolerance decreases as the Pr content increases.

Mechanical properties.— Mechanical properties is another feature to be considered for applications of the proton conducting perovskites as electrolytes supported PC-SOFC or as H_2 separation membranes. The mechanical strength of dense samples must be evaluated. SPT load vs. LVDT displacement curves obtained in air at room temperature, are plotted in Figure 7a for all compositions. In all cases, the specimens present an initial no-linear region followed by a linear rising in load until the brittle fracture. Figure 7b shows the fracture load and the mechanical stiffness evaluated by the slope of the linear fitting. Two displacements were measured during the SPT tests: puncher movement which is representative of the upper side of the disk and direct contact with the bottom side in contact with LVDT. The last one is independent of elastic indentation between ball and the specimen and reproduces more accurately the elastic bending behavior of the disk. Partial unloadings were performed in order to evaluate the pure linear elastic behavior. For each case, the slope of the linear fitting during unloading is representative of Young's modulus, only affected by geometric parameters.[47] Taking into account the porosity according to Figure 3c, the increasing elastic stiffness is larger than that expected by porosity reduction.[53] Within the porosity range (below of 8%), the reduction of elastic properties compared to that of full dense material should be lower than that observed. Analyzing stiffness for $BaCe_{0.8}Pr_{0.2}O_{3-\delta}$ and $BaCe_{0.6}Pr_{0.4}O_{3-\delta}$ with similar porosity, it

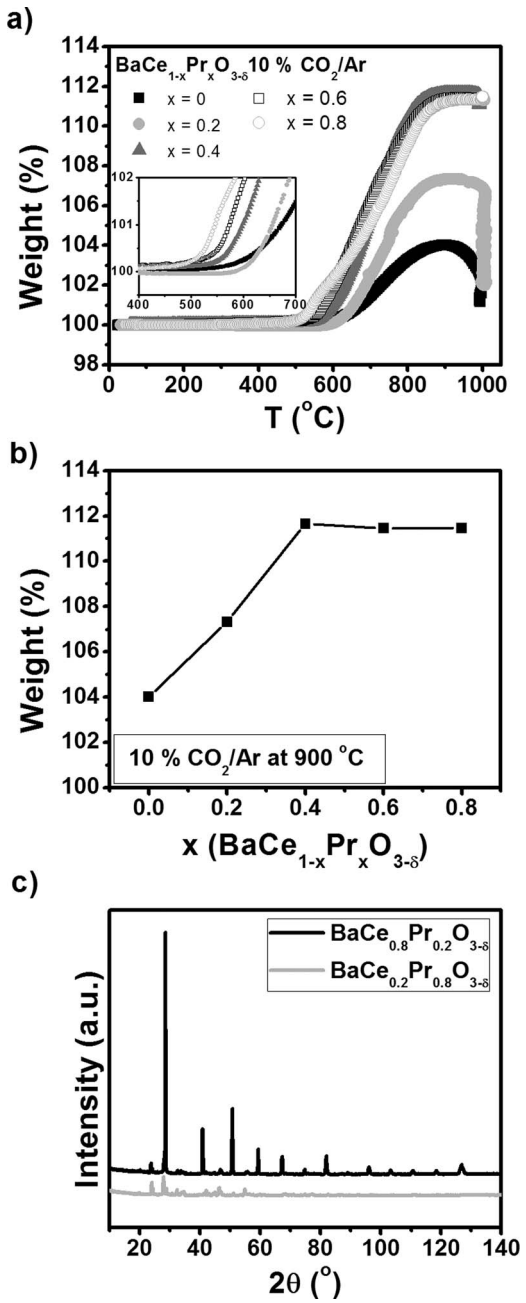

Figure 6. a)% Weight as function of temperature under 10% CO_2/Ar, for all compositions. b)% Weight gain as function Pr content. c) XRD patterns of $BaCe_{0.8}Pr_{0.2}O_{3-\delta}$ and $BaCe_{0.2}Pr_{0.8}O_{3-\delta}$ after cooled in Ar collected under the same scan conditions.

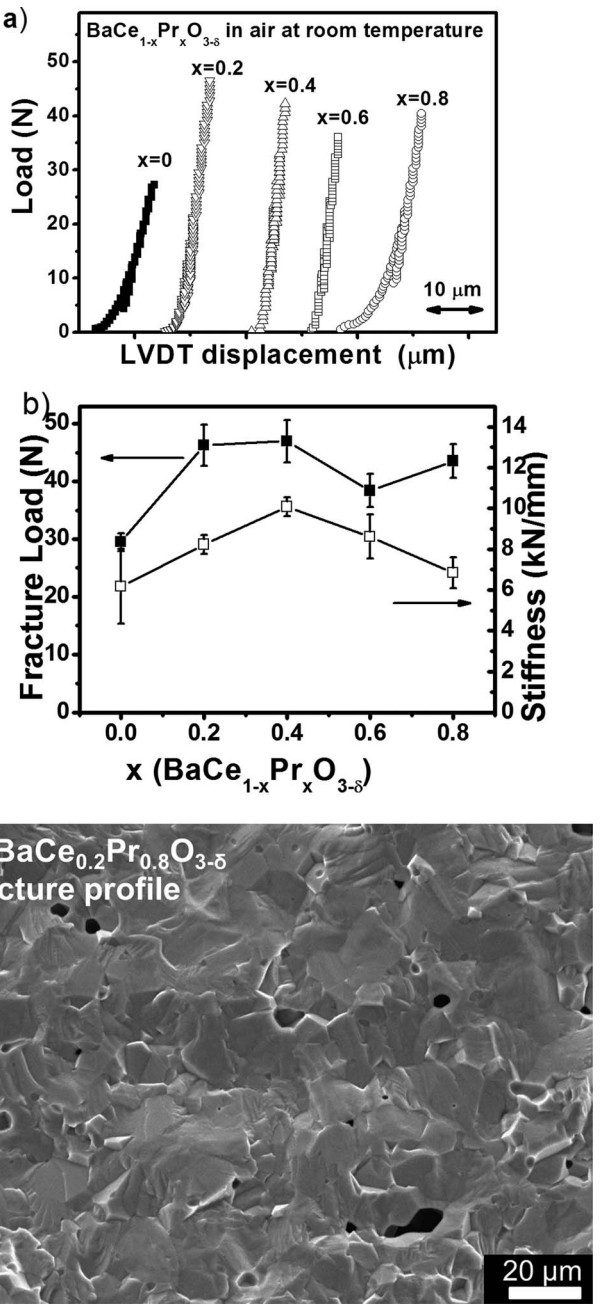

Figure 7. a) Load – LVDT displacement curves in air at room temperature for all compositions b) Fracture load and mechanical stiffness in function of Pr content of the dense pellets in air at room temperature. c) SEM image of $BaCe_{0.2}Pr_{0.8}O_{3-\delta}$ fracture profile.

indicates that the effect of Pr in this mechanical property is more than 60% than $BaCeO_{3-\delta}$.

Mechanical strength was evaluated through the fracture load reached during SPT test. Fracture load is proportional to stress fracture[47] affected by geometric factors. Taking into account that all specimens present the same dimension, the STP is an useful technique for comparative purposes. Figure 7b shows a maximum value of the fracture load for x = 0.2 and 0.4 samples.

Two microstructural features can affect the mechanical properties in ceramics: the porosity and the grain size distribution. While structural ceramics reduces strength with grain size increasing[53] some ceria ceramics have shown similar or inverse behavior depending on doping content.[47] On the other hand, the changes of porosity are not enough to explain the variation of fracture load. No secondary reinforcement phases were detected in order to explain the enhanced stiffness or strength. Fractured samples reveal typical macroscopic brittle fracture in mode I[48] obtaining two, three or four broken pieces divided from radial cracks from the center. In addition, neither plastic indentation nor other macroscopic plastic damage were found. SEM images of fractured surfaces shown in all cases mostly cleavage fractures and only few isolated intergranular grains fractures (Figure 7c, for $BaCe_{0.2}Pr_{0.8}O_{3-\delta}$). From fracture topography comparison between samples of different compositions, it is noted that the grain size would not affect the ratio between transgranular/intergranular fractures. Summarizing, Pr doping improves the mechanical properties of barium cerate due to the reinforcing of grain boundaries in spite of grain growth.

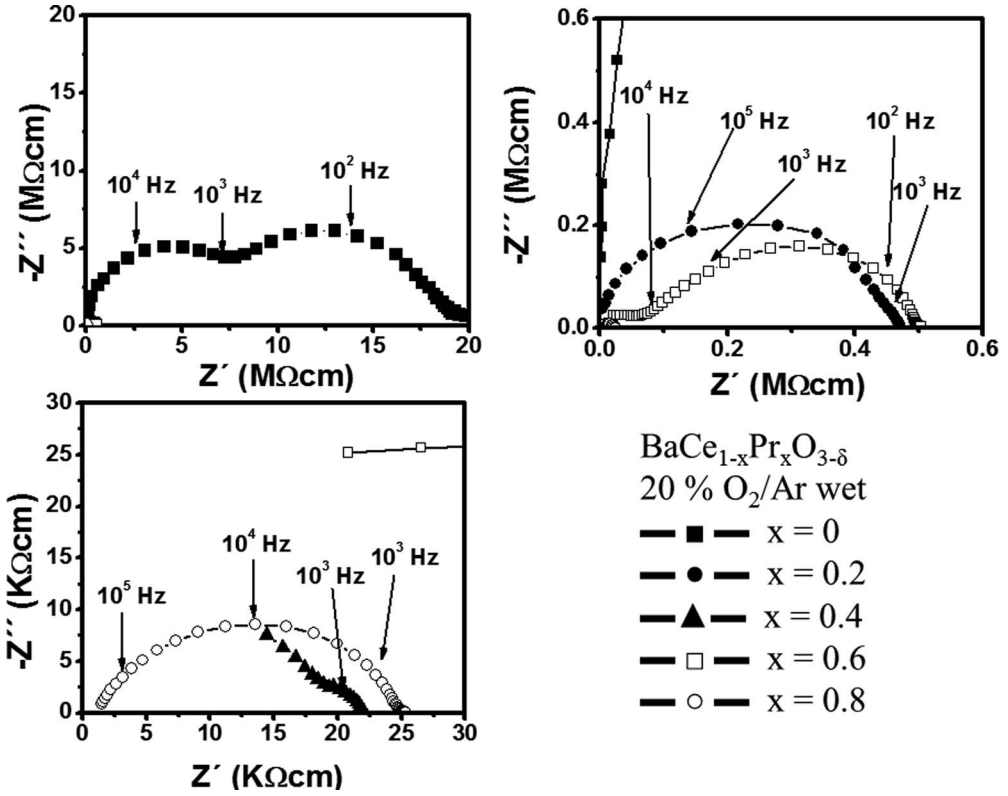

Figure 8. Nyquist plots of EIS spectra for the electrolytes obtained at 200°C in wet synthetic air.

Electrical conductivity.— A key parameter to characterize the PC-SOFC electrolyte is to evaluate the ionic conductivity at operation conditions. If the electronic transport number (t_e) is negligible compared with the ionic transport (t_i) number (proton or O ions), the total electrical conductivity (σ) is a representative measurement of the ionic conductivity. Determination of electrical conductivity is possible from EIS measurements. The electrochemical impedance due to ionic conductivity presents two contributions, the high frequency referred to bulk transport (b) and the low frequency corresponding to transport through grain boundary (gb). Figure 8 show the Nyquist plots of the $BaCe_{1-x}Pr_xO_{3-\delta}$ electrolytes in wet synthetic air at 200°C. At low temperatures, the two arcs could be distinguished. These arcs were fitted using an electrical equivalent circuit considering two series circuits, each of them with a resistance in parallel with a phase constant element (Rcpe). The electrolyte contributions move to highest frequencies and the resistances decrease as the temperature increases. Then, at temperatures over 300°C the overall electrolyte resistance is obtained from the interception of the impedance spectra with the real axis at high frequencies.

Figure 9a shows the Arrhenius plot of total electrolyte conductivity ($\sigma = \sigma_b + \sigma_{gb}$, where σ_b is bulk conductivity and σ_{gb} the grain boundary contribution) measured in wet air (2% H_2O). Pr doping improves the total conductivity of $BaCeO_{3-\delta}$ decreasing the electrolyte resistance between one and two orders of magnitude and shifting the maximum frequencies of relaxation to higher values. This result is similar to that reported by Sharova et al,[54] where the 15% of Pr and Sm doping increased the total conductivities 100 and 5 times more than that of $BaCeO_{3-\delta}$, respectively. The effect of Pr doping was evaluated also in $BaZrO_3$ proton conductor.[55,56] In these materials, the Pr-doping produces mixed conductor materials, where electrons and electron-holes are minority charge carriers and the defects concentration is dominated at low temperature by protons and at high temperature by oxygen vacancies. These authors suggest that electron hole conductivity is dominating at high pO_2, and proton conductivity becomes more significant at low temperature, low pO_2 and wet conditions,[56] whereas the n-type conductivity could be significant at low pO_2 and high temperatures. For $BaCe_{1-x}Pr_xO_{3-\delta}$ series, the increment of total conductivity is no linear with Pr content (See Figure 9b). This behavior is similar to the mechanical strength (see Figure 7b). The bulk contribution to conductivity limits the total conductivity at low Pr content, whereas the transport trough grain boundary is the controlling mechanism for Pr-rich samples.

The activation energy for undoped $BaCeO_{3-\delta}$ ($E_a = 0.81$ eV) is similar to literature values previously reported ($E_a = 0.79$ eV).[16] The Pr-doped perovskites present activation energies between 0.42 to 0.57 eV, whereas the values for Y, Zr partial substituted compounds are between 0.66 and 0.78 eV.[38] In a similar way to other $BaCeO_{3-\delta}$ lanthanides doped compounds, the activation energy decreases with doping concentration suggesting a change of the conduction mechanism due to the change of the transfer number of the effective charge carriers' (holes, protons and oxygen ions).[16,23,57] Although the change in activation energy suggests that the electron transport number increases with Pr doping. The total conductivities in wet air for $BaCe_{0.9}Ln_{0.1}O_{3-\delta}$ (Ln = Nd, Gd and Y) extracted from,[57] were included in Figure 9a for comparison. The lower conductivities for Pr-doped compounds related to other lanthanides doped proton conductors indicates a lower electronic contribution in $BaCe_{1-x}Pr_xO_{3-\delta}$ compounds compared with other lanthanides. For example, at 200°C, the electrical conductivity of $BaCe_{0.6}Pr_{0.4}O_{3-\delta}$ is one order of magnitude lower than that of $BaCe_{0.85}Gd_{0.15}O_{3-\delta}$. Similar conductivity values to Gd-doped have been reported for cerates doped whit Sm, Yb, Tb and Y, whereas slightly lower conductivities were founded for La and Nd-doped.[23,57] Therefore, diminishing the electronic contribution, the faradaic losses of efficiency are also reduced. That is an advantage for Pr-doped compounds compared with other lanthanide-doped cerates.

Considering the thermodynamic stability results previously discussed, the electrolyte resistance in wet 10% H_2/Ar flow was studied only for $BaCeO_{3-\delta}$ and $BaCe_{0.8}Pr_{0.2}O_{3-\delta}$ compositions. Figure 10a and 10b shows the Arrhenius plot for the total electrolyte conductivity

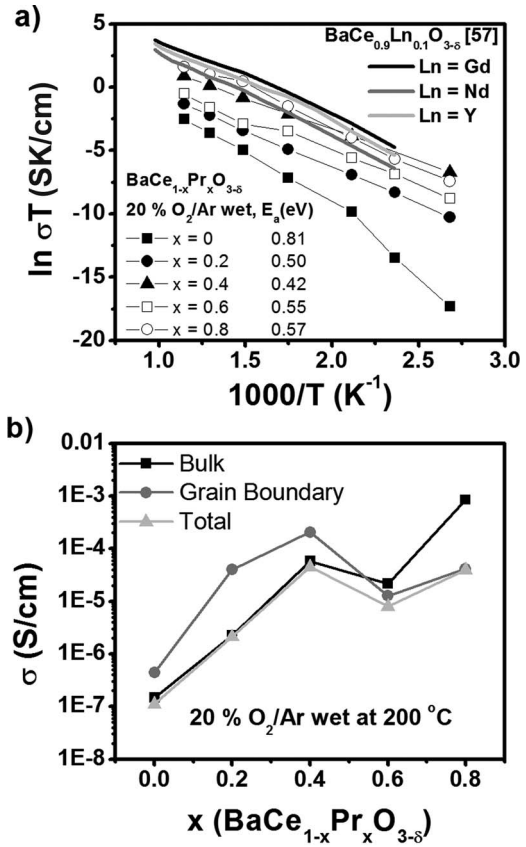

Figure 9. a) Arrhenius plot for each composition. Data for $BaCe_{0.9}Ln_{0.1}O_3$ (Ln = Nd, Gd and Y) from[57] are included for comparison. b) Electrolyte conductivity ($\sigma_t = \sigma_b + \sigma_{gb}$) obtained in wet synthetic air as a function of Pr content at 200°C.

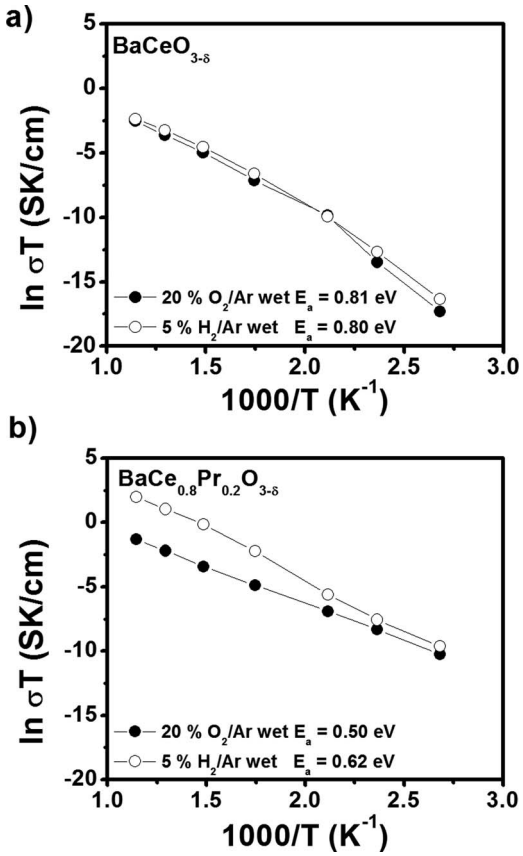

Figure 10. Comparison of Arrhenius plot of total electrolyte conductivity as a function of temperature obtained in wet synthetic air and wet 10% H_2/Ar for a) $BaCeO_{3-\delta}$ and b) $BaCe_{0.8}Pr_{0.2}O_{3-\delta}$.

obtained in wet synthetic air and wet 10% H_2/Ar for $BaCeO_{3-\delta}$ and $BaCe_{0.8}Pr_{0.2}O_{3-\delta}$, respectively.

$BaCeO_{3-\delta}$ presents practically the same conductivity in both atmospheres, while $BaCe_{0.8}Pr_{0.2}O_{3-\delta}$ increases its conductivity 20 times under reducing atmosphere at 600°C. The increases of conductivity for $BaCe_{0.8}Pr_{0.2}O_{3-\delta}$ composition under reducing atmosphere was also reported by Wang et al.[58] From EMF measurement in concentration cells, these authors propose for $BaCe_{0.8}Pr_{0.2}O_{3-\delta}$ an electron-hole conduction mechanism dominating in hydrogen-free atmosphere and a proton-ionic conduction controlling transport in wet hydrogen atmosphere. Wang et al.[58] assume that the increase of the total conductivity, in about one or two orders of magnitude, under H_2 containing atmosphere is due to the enhance of $OH^{\cdot}$ ionic charge carriers concentration. They also assume that some electronic conductivity can be present due to the mixed chemical valence of Pr (+4/+3) ions. On the other hand, Sharova et al.[54] demonstrate the existence of electron charge carrier at high temperature and low pO_2 for both $BaCeO_{3-\delta}$ and Pr- doped compound. They propose that at 900°C these oxides loss oxygen in reducing hydrogen atmosphere rising the electron defects concentration and therefore the electron conduction. Then, as the mobility of electrons is higher than that of ions, the emergence of electrons must lead to a sharp increase on conductivity in reducing atmospheres. The oxygen non stoichiometry of $BaCeO_{3-\delta}$ remains practically constant until 800°C regardless the atmosphere (see Figure 4b). However, the $BaCe_{0.8}Pr_{0.2}O_{3-\delta}$ is partially reduced below 600°C under H_2-containing atmosphere (see Figure 4a), which increases oxygen vacancies and electronic charge carriers. Then, the rise of conductivity in reducing atmosphere for $BaCe_{0.8}Pr_{0.2}O_{3-\delta}$ could be ascribed to the existence of electronic charge carriers. Similar results were found for high Pr-doping $BaCe_{0.8-x}Pr_xGd_{0.2}O_{2.9}$, which was proposed as cathode materials due to their mixed H-ionic and electronic conductivities.[59] Only considering this information, it is difficult to assign the increment of conductivity to either H-ionic conductivity or O-ionic conductivity or electronic conductivity. Further studies on blocking electrodes could give the key to understand if the cause of this improvement is due only to the increase of electronic transfer number or to the ionic transport. At this stage of research, the improvement of sintering capabilities and mechanical resistance together with a reasonable H_2 and CO_2 tolerance makes the $BaCe_{0.8}Pr_{0.2}O_{3-\delta}$ compound an interesting material to be further researched. The dependence of conductivity as a function of pO_2 in a whole range of temperatures should be determined in detail in order to understand conduction mechanisms and therefore possible applications.

Conclusions

In this work, the effect of partial substitution of Ce by Pr ions in $BaCe_{1-x}Pr_xO_{3-\delta}$ (x = 0, 0.2, 0.4, 0.6 and 0.8) was studied with the aim to improve sintering, mechanical properties, thermodynamic stability under different atmospheres and proton conduction.

The Pr content decreases the lattice parameters, improves the sintering capacity and increases the conductivity under wet oxidant atmosphere. However, the stability under reducing and carbon dioxide atmospheres decreases.

Dense $BaCe_{0.8}Pr_{0.2}O_{3-\delta}$ with low porosity (5 ± 1%) coarse grain size (3.26 μm) was reached at 1350°C. The mechanical properties were improved in comparison with undoped sample, e.g. stiffness and fracture load increase almost 30% and 56%, respectively. This composition also shows a good stability under oxidizing and reducing atmosphere, and slightly higher CO_2 tolerance range (decomposition start at 550°C). The little increase of CO_2 tolerance for $BaCe_{0.8}Pr_{0.2}O_{3-\delta}$ compared with undoped sample could be due to the fact that the

increase of grain size decreases the carbonization rate. The electrical conductivity of $BaCe_{0.8}Pr_{0.2}O_{3-\delta}$ reaches values of 2.12×10^{-6} and 3.07×10^{-4} Scm^{-1} at 200 and 600°C, respectively.

Acknowledgments

This work was supported by Microscopy Service - Materials Characterization Department and Metals Division, CAB - CNEA (Centro Atómico Bariloche- Comisión Nacional de Energía Atómica), CONICET (Consejo Nacional de Investigaciones Científicas y Técnicas), UNCu (Universidad Nacional de Cuyo), ANPCyT (Agencia Nacional de Promoción de Ciencia y Tecnología), LNLS-Camphinas (Bazilian National Laboratory of Synchrotron Light).

References

1. K. Huang, J.-H. Wan, and J. B. Goodenough, *J. Electrochem. Soc.* **148**, A788 (2001).
2. M. Mamak, N. Coombs, and G. Ozin, *J. Am. Chem. Soc.* **122**, 8932 (2000).
3. H. Zhang, H. Liu, Y. Cong, and W. Yang, *J. Power Sources* **185**, 129 (2008).
4. E. Fabbri, D. Pergolesi, and E. Traversa, *Chem. Soc. Rev.* **39**, 4355 (2010).
5. A. B. Stambouli and E. Traversa, *Renew. Sust. Energ. Rev.* **6**, 433 (2002).
6. F. Lefebvre-Joud, G. Gauthier, and J. Mougin, *J. Appl. Electrochem.* **39**, 535 (2009).
7. S. Haile, *Acta. Mater.* **51**, 5981 (2003).
8. L. Bi, S. Zhang, L. Zhang, Z. Tao, H. Wang, and W. Liu, *Int. J. Hydrogen Energy* **34**, 2421 (2009).
9. H. Iwahara, H. Uchida, and K. Morimoto, *J. Electrochem. Soc.* **137**, 462 (1990).
10. T. Norby, *Solid State Ionics* **125**, 1 (1999).
11. C. Zuo, S. Zha, M. Liu, M. Hatano, and M. Uchiyama, *Adv. Mater.* **18**, 3318 (2006).
12. D. Medvedev, A. Murashkina, E. Pikalova, A. Demin, A. Podias, and P. Tsiakaras, *Progr. Mater. Sci.* **60**, 72 (2014).
13. J. F. Liu and A. S. Nowick, *Solid State Ionics* **50**, 131 (1992).
14. L. Pelletier, A. McFarlan, and N. Maffei, *J. Power Sources* **145**, 262 (2005).
15. H. Iwahara, *Solid State Ionics* **77**, 289 (1995).
16. E. Gorbova, V. Maragou, D. Medvedev, A. Demin, and P. Tsiakaras, *J. Power Sources* **181**, 207 (2008).
17. K. H. Ryu and S. M. Haile, *Solid State Ionics* **125**, 355 (1999).
18. R. Glockner, M. S. Islam, and T. Norby, *Solid State Ionics* **122**, 145 (1999).
19. N. Bonanos, *Solid State Ionics* **145**, 265 (2001).
20. A. Sammells, R. Cook, J. White, J. Osborne, and R. MacDuff, *Solid State Ionics* **52**, 111 (1992).
21. K. D. Keuer, *Annu. Rev. Mater. Res.* **33**, 333 (2003).
22. H. Iwahara, H. Uchida, K. Ono, and K. Ogaki, *J. Electrochem. Soc.* **135**, 529 (1988).
23. M. Amsif, D. Marrero-López, J. C. Ruiz-Morales, S. N. Savvin, and P. Núñez. *J. Power Sources* **196**, 9154 (2011).
24. J. Kikuchi, S. Koga, K. Kishi, M. Saito, and J. Kuwano, *Solid State Ionics* **179**, 1413 (2008).
25. X. T. Su, Q.-Z. Yan, X.-H. Ma, W.-F. Zhang, and C.-C. Ge, *Solid State Ionics* **177**, 1041 (2006).
26. C. Zhang and H. Zhao, *Solid State Ionics* **206**, 17 (2012).
27. F. Giannici, A. Longo, K.-D. Kreuer, A. Balerna, and A. Martorana, *Solid State Ionics* **181**, 122 (2010).
28. Y.-J. Gu, Z.-G. Liu, J.-H. Ouyang, F.-Y. Yan, and Y. Zhou, *Electrochim. Acta* **105**, 547 (2013).
29. D. Medvedev, V. Maragou, T. Zhuravleva, A. Demin, E. Gorbova, and P. Tsiakaras, *Solid State Ionics* **182**, 41 (2011).
30. N. Nasani, P. A. N. Dias, J. A. Saraiva, and D. P. Fagg, *Int. J. Hydrogen Energy* **38**, 8461 (2013).
31. M. Amsif, D. Marrero-López, J. C. Ruiz-Morales, S. N. Savvin, and P. Núñez, *J. Eur. Cer. Soc.* **34**, 1553 (2014).
32. Y. Guo, R. Ran, and Zo. Shao, *Int. J. Hydrogen Energy* **35**, 5611 (2010).
33. G. Chiodelli, L. Malavasi, C. Tealdi, S. Barison, M. Battagliarin, L. Doubova, M. Fabrizio, C. Mortalo, and R. Gerbasi, *J. Alloy. Compd.* **470**, 477 (2009).
34. A. Roberts and E. Garboczi, *J. Am. Ceram. Soc.* **83**, 3041 (2000).
35. K. D. Kreuer, *Solid State Ionics* **97**, 1 (1997).
36. D. Shima and S. M. Haile, *Solid State Ionics* **97**, 443 (1997).
37. N. Zakowsky, S. Williamson, and J. T. S. Irvine, *Solid State Ionics* **176**, 3019 (2005).
38. P. Sawant, S. Varma, B. N. Wani, and S. R. Bharadwaj, *Int. J. Hydrogen Energy* **37**, 3848 (2012).
39. S. Ricote, N. Bonanos, and G. Caboche, *Solid State Ionics* **180**, 990 (2009).
40. Y. Guo, R. Ran, and Z. Shao, *Int. J. Hydrogen Energy* **35**, 10513 (2010).
41. K. Knight, *Solid State Ionics* **145**, 275 (2001).
42. K. Knight, *Mater. Res. Bull.* **30**, 347 (1995).
43. http://www.ill.eu/sites/fullprof/.
44. S. Megel, K. Eichler, N. Trofimenko, and S. Hoehn, *Solid State Ionics* **177**, 2099 (2006).
45. http://compdent.uthscsa.edu/dig/itdesc.html.
46. A. Caneiro, P. Bavdaz, J. Fouletier, and J. P. Abriata, *Rev. Sci. Instrum.* **53**, 1072 (1982).
47. K. Sato, H. Yugami, and T. Hashida, *J. Mat. Sci.* **39**, 5765 (2004).
48. Z. Xiong, W. Jiang, Y. Shi, A. Kawasaki, and R. Watanabe, *Mat. Trans.* **46**, 631 (2005).
49. Zview versión 2.9b. Copyright 1990–2005, Scribner Associates, Inc. D. Johnson.
50. R. D. Shannon, *Acta Crystallogr.* **A32**, 751 (1976).
51. A. Le Bail, *Powder Diffr.* **20**, 316 (2005).
52. A. Magrasó, C. Frontera, A. Gunnaes, A. Tarancon, D. Marrero-Lopez, T. Norby, and R. Haugsrud; *J. Power Sources* **196**, 9141 (2011).
53. R. W. Rice. Microstructure Dependence of Mechanical Behavior of Ceramics. Treatise Mat. Sci. Tech., *Properties and Microstructure 11* (R. C. McCrone ed). Academic Press, New York, 1997, 199–381.
54. N. V. Sharova, V. P. Gorelov, and V. B. Balakireva. *Russ. J. Electrochem.*, **41**, 665 (2005).
55. S. Gill, R. Kannan, N. Maffei, and V. Thangadurai, *RSC Advances*, **3**, 3599 (2013).
56. A. Magraso, C. Kjølseth, R. Haugsrud, and T. Norby, *Int. J. Hydrogen Energy* **37**, 7962 (2012).
57. M. Amsif, D. Marrero-Lopez, J. C. Ruiz-Morales, S. N. Savvin, M. Gabas, and P. Nunez *J. Power Sources* **196**, 3461 (2011).
58. M.-Y. Wang and L-.G. Qiu, *Chin. J. Chem. Phys.*, **21**, 286 (2008).
59. R. Mukundan, P. K. Davies, and W. L. Worrell, *J. Electrochem. Soc.* **148**, A82 (2001).